MNRAS **000**, 1–13 (2016) Preprint 26 June 2017 Compiled using MNRAS LATEX style file v3.0

Radiation and supernovae feedback during the epoch of reionization with EMMA

Nicolas Deparis[1]★, Dominique Aubert[1], Pierre Ocvirk[1] and Nicolas Gillet[2]
[1] *Observatoire Astronomique de Strasbourg, CNRS UMR 7550, Universite de Strasbourg, Strasbourg,France*
[2] *Scuola Normale Superiore, Piazza dei Cavalieri 7, I-56126 Pisa, PI, Italy*

Accepted XXX. Received YYY; in original form ZZZ

ABSTRACT

We aim at investigating the role of stellar feedback in large scale cosmological simulations of reionization, in the regime of kpc resolution. The link between star formation, ionizing sources and supernovae feedback at high redshift is examined using `EMMA` , a radiative-hydrodynamics (RHD) code with adaptive mesh refinement (AMR). We present a new supernovae feedback model based on kinetic energy injection and compare this model to simple thermal injection scheme. We show that this model is able to regulate star formation on a wide range of halo masses. We compute the average velocity of galactic winds around halos and we show that our feedback model is able to efficiently generate galactic outflows for halos with masses between $10^8 M_\odot$ and $10^{11} M_\odot$.

We also observe baryon outflows due to photo-evaporation by radiative feedback for halos less massive than $10^9 \mathrm{M}_\odot$. We then investigate the influence of the various feedbacks on the reionization process and show that even in the presence of a significant regulation of star formation, the different feedback mechanisms have a small impact the simulated reionization history.

Key words: cosmology: dark ages, reionization, first stars - methods: numerical

1 INTRODUCTION

Stellar feedback is a crucial ingredient in the process of galaxy formation. By changing the state of the inter-stellar medium (ISM), stellar feedback introduces a highly nonlinear coupling between the accretion and outflow of gas material in dark matter haloes which is regulating the star formation process in galaxies. Supernovae explode inside star-forming regions and blow away the gas that is needed for the future generation of stars. Therefore, the more efficient is the star formation process, the more efficient is the feedback and the less efficient is the subsequent star formation. These effects are especially important during the epoch of reionization when the star formation process begins. Understanding the star formation process is therefore crucial during this period in order to correctly follow the build-up of the first generation of ionizing sources.

Supernova feedback was introduced in cosmological simulations mainly for two reasons. First it has been implemented to compensate the overcooling problem when the accretion rate of baryons onto dark matter halos is too high in the absence of feedback, leading to galaxies with far larger masses compared to observed ones.

Secondly, supernova feedback was studied to reproduce observed galactic outflows (Veilleux et al. 2005) that have been found to be difficult to reproduce in simulations.

Even if supernova feedback has been extensively investigated for more than two decades (Katz 1992; Navarro & White 1993), its numerical implications are still unclear. Different kinds of subgrid modelling have been developped for the supernova feedback with different levels of complexity depending of the spatial resolution of the simulations (Katz 1992; Navarro & White 1993; Springel & Hernquist 2003; Stinson et al. 2006; Dubois & Teyssier 2008; Dalla Vecchia & Schaye 2012). A few projects have been undertaken to compare the feedback implementations (Kimm et al. 2015; Rosdahl et al. 2016), but there is still no consensus about the right way to deal with it in simulations.

In this work, we focus on the reionization process and we consider that stars in star-forming galaxies are the main emitters of ionizing photons[1]. It is still unclear how UV

★ E-mail: nicolas.deparis@astro.unistra.fr

[1] It has been shown recently that accreting black holes in Active Galactic Nuclei (AGNs) could contribute significantly to the UV

radiation can escape the hosting dark matter haloes: the way photons propagate through the gas is highly dependent to the local density which depends on the stellar feedback. Therefore, there is a direct link between star formation, stellar feedback and ionizing sources during the reionization process. Understanding where and how stars form is primordial to understand which radiative sources dominate the photon budget.

The main difficulty is the underlying multi-scale problem where supernova explosion occur at sub-parsec scale while creating gas outflow at scales up to several hundreds of kiloparsecs and Reionization occurs on tens of Mpc scales. This is especially hard to tackle in simulations of the Reionization process where we ideally want to simulate a very large volume to correctly sample the cosmic variance : Iliev et al. (2014) have indeed shown that a volume of 50-100 cMpc is needed to correctly follow the reionization process. Considering such volumes and the current super-computing facilities, simulations are still way far to resolve the formation and evolution of individual stars while being able to model the large-scale reionization. Recent state-of-the art examples include the CODA (Ocvirk et al. 2015), the CROC (Gnedin 2014) or the upcoming CODA-EMMA (Aubert et al., in prep) simulations. All these projects aim at making predictions on populations of galaxies at $z > 6$ during the Reionization epoch and all this projects were massive high-performance computing challenges, with number of resolution elements in the $10^{10} - 10^{11}$ range. Such simulations are necessary to solve the tension that necessarily arises between the opposite requirements of a large simulated volume and a decent spatial resolution. All the aforementioned work used similar 64Mpc/h volumes with spatial resolutions in the $0.1 - 1$ kpc range: such spatial sampling is insufficient to model directly the in-situ impact of supernova feedback on galactic gas and rely on subgrid modeling. Likewise, it is evident that such simulations are unable to track the detailed structure of galaxies at these epoch.

On the other hand, the inclusion of such feedback is necessary as it impacts the gas properties (density, metallicity, kinematics) and stellar formation processes on spatial scales that are being resolved by these simulations. In addition, it has been found that population properties, such as the luminosity functions can be properly reproduced (Ocvirk et al. 2015; Gnedin 2014). Such studies cannot compete in terms of resolution with resolved studies (such as e.g. Wise & Cen (2009); Trebitsch et al. (2015); Rosdahl et al. (2016); Kimm et al. (2017)) but their goal is not to model the small scale physics at play but rather to be able to reproduce population and large-scale reionization properties. For the latter, the representativity of environments or the diversity of histories are expected to play a significant part (see e.g. Li et al. (2014)) : these assets cannot be obtained with resolved simulations of singled-out or zoomed galaxies.

As a consequence, it is important to understand how the different types of feedback interact in such kind of large-scale and moderately resolved simulations. It's notably important considering objects close to the resolution limit ($10^8 - 10^9 M_\odot$ in our case) : such halos are numerous, heavily affected by photo-suppression ((Ocvirk et al. 2015)) and susceptible to outflows and large radiative escape fractions. Overall, their contribution to state-of-the art Reionization simulations must be understood and in particular the coupling between the different types of feedback. The current work is presented in this optics: using resolutions similar to the aforementioned large scale simulations, we aim at understanding how the global reionization properties and the galaxy populations produced by such models are shaped by the different feedbacks (radiative and supernova).

We introduce the cosmological code `EMMA` in Sec 2.1 as well as our implementation of our star formation and evolution model in Sec. 2.2. An important part of this evolution model is the supernovae feedback scheme, so we present two implementations of supernovae feedback: a classic direct thermal injection described in Sec. 2.3.1 and an original kinetic model constrained by the AMR oct-tree structure of `EMMA` presented in Sec. 2.3.2. We introduce the direct thermal injection implementation for comparison purpose only, as we already know that it will suffer of high radiative losses (Katz 1992). We quantify the influence of the choice of supernovae model on star formation using a set of global variables like the star formation history (SFH) or ionization history and conclude that our kinetic model is able to efficiently regulate star formation in our resolution regime. We also investigate the influence of our models parameters on the stellar and baryonic content of halos, as well as their UV emissivity: in particular we discuss the role of the different mass classes to the Reionization and SFH at the resolution of large scale simulations.

2 METHODOLOGY

In this section we describe our modeling of cosmic reionization with the `EMMA` code. We will take particular care to explain our supernova feedback implementation as well as our star formation prescription. We will finally give our initial set-up and the description of the different simulations studied in this paper.

2.1 Code description

We perform cosmological radiative hydrodynamic simulation with the `EMMA` (Aubert et al. 2015) code, an Adaptive Mesh Refinement (AMR) based code, designed to study the Epoch of Reionization (EoR). The code follows the evolution of three distinct physics: the colisionless Dark Matter (DM) dynamics, the gas dynamics, and the radiative transfer of ionizing photons with all the different modules self-consistently coupled to each other.

`EMMA` uses a fully treated three AMR description (Khokhlov 1998). The collisionless dynamics – dark matter and stars – use a particle based representation (Hockney & Eastwood 1981). The gravitational density field is determined from the particle using a Cloud In Cell (CIC) projection. The Poisson equation is solved using a multigrid relaxation method on the base level, and a Gauss-Seidel relaxation on the sub levels. The hydrodynamics solver is based on a piecewise linear method a la MUSCL-Hancock driven

photon budget (Giallongo et al. 2015; Haardt & Madau 2012; Chardin et al. 2017; D'Aloisio et al. 2016) However, star-forming galaxies are still the main candidates (Bouwens et al. 2015)

by HLLC Riemann solvers (Toro 1997). Finally, the radiation propagation is solved using a moment-based description, with the M1 closure approximation (Aubert & Teyssier 2008; Aubert & Teyssier 2010).

2.2 Star formation

In the two following subsections, we introduce our star formation and feedback models, as well as their free parameters. We are only focusing here on the general model implementation and all details about free parameters values used in this study can be found in Sec. 2.4.

To flag star forming regions, we use a simple overdensity criterion δ . For every cells above this threshold, we compute the Star Formation Rate (SFR) :

$$\dot{\rho} = \epsilon_{SF} \frac{\rho_g}{t_{\rm ff}}, \tag{1}$$

with ϵ_{SF} an efficiency parameter, ρ_g the local gas density and $t_{\rm ff}$ a local free fall time expressed as :

$$t_{\rm ff} = \sqrt{\frac{3\pi}{32 G \rho_g}}, \tag{2}$$

This leads to $\dot{\rho} \propto \rho_g^{1.5}$ close to the Schmidt-Kennicutt law (Kennicutt 1998).

Based on this SFR, we express the total mass to convert from gas to stars depending on the volume of the current cell dv and the current timestep dt:

$$M_\star = \dot{\rho} \cdot dv \cdot dt. \tag{3}$$

We then follow Rasera & Teyssier (2006), and define a stellar quantum mass of $m_\star$. Using $n_\star = \frac{M_\star}{m_\star}$, we compute an average number $n_\star$ of stellar particles to create. We finally draw the final number of particles $N_\star$ to inject in a Poisson law of parameter $n_\star$.

The star particles that are created are placed randomly in the cell volume with a velocity corresponding to the local gas velocity plus a component with a random direction and a random amplitude bound by the local sound speed. During the process of star formation, the mass conservation is obviously respected.

2.3 Supernovae feedback

In this section, we discuss how we implement two different feedback methods. For both methods we dispose of a given amount of energy E_{SN} to inject in the hydrodynamical solver changing either internal or kinetic energy of the gas around the explosion.

2.3.1 Thermal feedback implementation

The thermal feedback model is the simplest way to inject energy. Such an implementation consists in the energy injection by modifying the local pressure:

$$\Delta P = \frac{E_{SN}}{dV} (\gamma - 1), \tag{4}$$

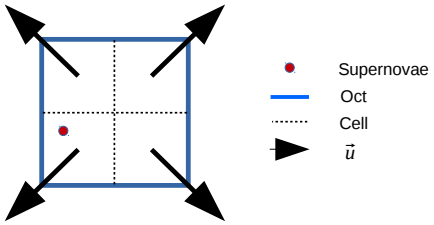

Figure 1. Kinetic energy injection scheme. No matter where the particle is in the oct, the explosion occurs radially from the center of the oct.

where dV is the cell volume and the adiabatic index $\gamma = 5./3$.

Once the energy injection has been done, a fraction f_r of the stellar particle mass is returned and put back into the cell. The total mass return is $m_r = f_r \cdot m_\star$.

We use this feedback for comparison purpose only.

2.3.2 Kinetic feedback implementation

Historically, kinetic feedback was developed after it has been shown that thermal feedback suffers from high radiative losses and is inefficient to generate galactic outflows (Navarro & White 1993). Kinetic feedback consists into modifying the velocity of the gas in cells around the explosion instead of its internal energy. Its main advantage is that it override the conversion of heat into movement, highly inefficient when cooling processes are allowed.

But its main inconvenient its that it leads to a loss of resolution. Indeed, when a thermal scheme can heat an unique cell, kinetic needs to change the properties of the gas in a bigger number of cells to result in a spherical explosion. Moreover, the bigger the number of cells is, the more spherical the resulted blast wave will be. On an AMR grid, finding neighbor has a cost and the counter part of a rounder explosion is that the numerical cost of finding the considered cells will quickly rise. Furthermore, due to the parallel nature of computations in `EMMA` , if an explosion occurs at an edge of a processor domain, distributing the explosion along the cells will result in costly communications. In our case, we limit the number of cells in which the explosion occurs to 8 and, using the AMR oct-tree structure of `EMMA` , theses eight cells have to share the same parent oct. This almost reduce to zero the cost of the neighbor search, and totally avoid communication between processors. Moreover, this also allows us to be sure that cells where the feedback is computed are all at the same level of resolution, which ensure us a certain homogeneity in the explosion. A schematic view of our injection scheme is given in Fig. 1.

We divide the total available energy, uniformly into theses eight cells, so each cell receives,

$$e_{SN} = E_{SN}/8. \tag{5}$$

Finally, e_{SN} is used to change the gas velocity of each cell,

$$\Delta \overrightarrow{v_{gas}} = \sqrt{\frac{2 e_{SN}}{\rho_g . dV}} \vec{u}, \tag{6}$$

where $\vec{u}$ is the unit vector pointing radially from the center

Name	ϵ_{SF}	f_{esc}	Supernovae	ϵ_{SN}
noFEED	0.5%	0	-	0
noSN/ϵ_{SN} = 0	0.5%	0.4	-	0
ϵ_{SN} = 0.1	0.5%	0.4	Kinetic	0.1
ϵ_{SN} = 0.5	0.5%	0.4	Kinetic	0.5
ϵ_{SN} = 1	0.5%	0.4	Kinetic	1
Thermal	0.5%	0.4	Thermal	1
Kinetic/SF05	0.5%	0.4	Kinetic	1
SF2	2%	0.4	Kinetic	1
SF10	10%	0.4	Kinetic	1

Table 1. Simulations features investigated in this study. The parameters are: the identification run name, the star formation efficiency ϵ_{SF}, photon escape fraction f_{esc}, type of supernovae feedback method and the efficiency of supernovae feedback ϵ_{SN}. All theses runs share the same initial conditions described in Sec. 2.4.

of the oct. The mass is returned in the same way as for the thermal feedback except that each cell now receives one-eight of the total available mass.

2.4 Simulations parameters

Our stellar feedback model is intended to be used in large scale reionization simulation like CODA (Ocvirk et al. 2015). Such simulations are unique (e.g. $64 \cdot h^{-1}$ comoving Mega parsec (cMpc) cube , 4096^3 resolution elements for CODA) and cannot be used to test the stellar feedback parameters: for this purpose, we produce smaller boxes with equivalent resolutions. The goal of the set of simulations is to test our model and improve our understanding of the effects of stellar feedback parameters in large-scale cosmological simulations of the Reionization.

In the following, we consider a $(8 \cdot h^{-1}$ cMpc$)^3$ boxes $(\approx 12$cMpc$)^3$, resolved with 256^3 dark matter particles. This leads to a DM mass resolution of $3.4 \cdot 10^6 M_\odot$, and a spatial resolution of 46ckpc on the coarse grid. The mass resolution is then one level below the resolution of the CODA simulation, but the spatial resolution is improved by the AMR of `EMMA`. Initial Condition (IC) were generated with MUSIC (Hahn & Abel 2011) with a Planck Cosmology (Planck Collaboration et al. (2015) : $\Omega_m = 0.3175$, $\Omega_\nu = 0.6825$, $\Omega_b = 0.0490$, $H_0 = 67.11$, $\sigma_8 = 0.830$. The simulations start at redshift $z = 150$ and share the same set of displacement phases. The grid is refined according to a semi-Lagrangian scheme, i.e. the cell is flagged for refinement if its dark matter or baryon mass exceed 8 times the equivalent mass of a coarse cell filled with the average dark matter or baryon density: if $\rho \cdot dV \geq 8 \cdot \bar{\rho} \cdot dV_{coarse}$ where ρ can be the dark matter or the baryon density. The refinement is not allowed if the spatial resolution of the newly formed cells is under 500pc. In the goal to reduce the computational cost, we use a reduced speed of light of 10% of the real one, coupled with the Coarse Radiative Transport Approximation (CRTA) scheme implemented in the `EMMA` code (see Aubert et al. (2015)). This reduced speed of light is shown to provide results similar to the one obtained with the actual one (e.g. Deparis et al., in prep). The CRTA scheme propagates radiation at the coarse cell resolution (i.e. 46 comoving kpc in the current case) but

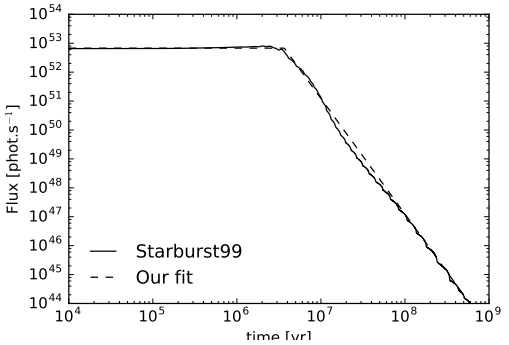

(a) Ionizing flux

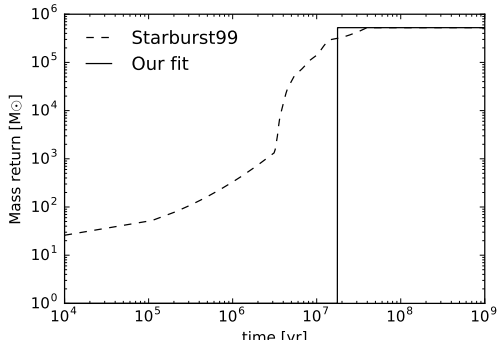

(b) Cumulative mass return

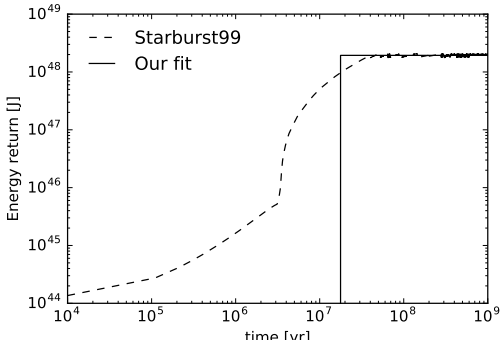

(c) Cumulative energy return

Figure 2. Our stellar model is calibrated with the Starburst99 model. The Starburst99 run considers a $10^6 M_\odot$ population with a Top Heavy IMF and a metalicity of Z=0.001. Our ionizing emissivity model (Fig. 2a) presents two phases, a constant emissivity one, and a decreasing one. The transition between theses two phases define the radiative lifetime $t_{\rm life}$. Mass (Fig. 2b) and energy (Fig. 2c) return from winds and supernovae are released instantaneously at the same time $t_{\rm SN}$.

photo-chemistry is performed at the finest resolution available (i.e. 500 pc in the current case).

We use a star formation over-density threshold of $\delta = 50$ and star formation efficiency parameter $\epsilon_{SF} = 0.5\%$. Our model for the ionizing emissivity of the star particles is calibrated using Starburst99 (Leitherer et al. 1999). Because our resolution does not allow to track real individual star particles, we consider that each star particle represents a stellar population of $7.2 \cdot 10^4 M_\odot$ with a Top-Heavy Initial

Mass Function (IMF) (exponent 1.3 for $0.1 < m/M_\odot \leq 0.5$,2.3 for $0.5 < m/M_\odot \leq 1$ and 1.6 for $1 < m/M_\odot \leq 100$) integrated from $0.1M_\odot$ to $100M_\odot$ and with a constant metallicity of $Z = 0.001$.

Since we are only considering hydrogen reionization, the Starburst99 spectrum is integrated on the energy range from 13.6eV to infinity corresponding to the ionizing spectrum of neutral hydrogen. The ionizing emissivity presents two regimes (See Fig. 2a) with a constant phase followed by a fast emissivity drop. During the constant emissivity phase, sources emit $S_0 = 1.55.10^{17}$ phot.sec^{-1}.kg^{-1}. We consider the radiative lifetime $t_{\rm life}$ of sources to be at the transition of theses two regimes: $t_{\rm life} = 3.67.10^6$Myr. After t_{life}, the sources still radiate with a number of photons that is a decreasing power law as a function of time ($S_{(t>t_{\rm life})} \propto t^{-4}$). The calculations are done using a monochromatic photons with a mean energy of $< h\nu >= 23.42$ eV, an energy weighted cross section of $\sigma_e = 2.35.10^{-22}$ m^2 and a number weighted cross section of $\sigma_i = 1.82.10^{-22}$ m^2.

Supernova feedback model are also calibrated using Starburst99 as it gives us access to the temporal evolution of the amount of mass (Fig. 2b) and energy (Fig. 2c) returned in the medium by the considered stellar population. We choose to inject the totality of the available energy instantaneously after a time $t_{\rm SN}$ which is defined as the time where 50% of all the energy from Starburst99 should be released. We use the total amount of energy released by winds and supernovae during the whole lifetime of the population. The quantity of energy injected in our model is regulated by an efficiency parameter ϵ_{SN}. We return a mass fraction f_r of the total particle mass when a supernova explodes. All the mass is released instantaneously at the same instant as the energy. In practice, our model parameters are: an injection time of $t_{\rm SN} = 17.7$ Myr, a total available energy of $E_{SN} = 2.47 \cdot 10^{42}$J.M$_\odot^{-1}$ and a mass return fraction of $f_r = 52.6\%$.

Tab. 1 presents a summary of the different runs performed in this study. It should be noted that we did not attempt to calibrate the simulations to satisfy observational constraints (here the star formation rate and ionization fraction history). The latter are given to indicate that the runs deliver reasonable results but given the small simulated volumes or the limited range of halo masses (the most massive halo has $M \approx 10^{11} M_\odot$), our simulation are known to lack the statistical representativity of objects, scales or environments. Enforcing an exact reproduction of observational constraints would be of limited scope and we focus rather on differential comparisons between runs using different physics.

3 TEMPERATURE AND DENSITY FIELDS AROUND THE MOST MASSIVE HALO

Our first diagnostic is purely qualitative and consists in looking at the density and temperature fields around a specific halo. We choose the most massive halo in the *noSN* simulation, which has a mass of M$= 1.10 \cdot 10^{11}$M$_\odot$, corresponding to a R_{200} radius of 21kpc at redshift $z = 6$. Fig. 3 represents a $214 \times 214 \times 6.5$ kpc slice at redshift $z = 6$, centered on this halo, for simulation without supernovae feedback (first row), with direct thermal injection (middle row) and with our kinetic model (bottom row).

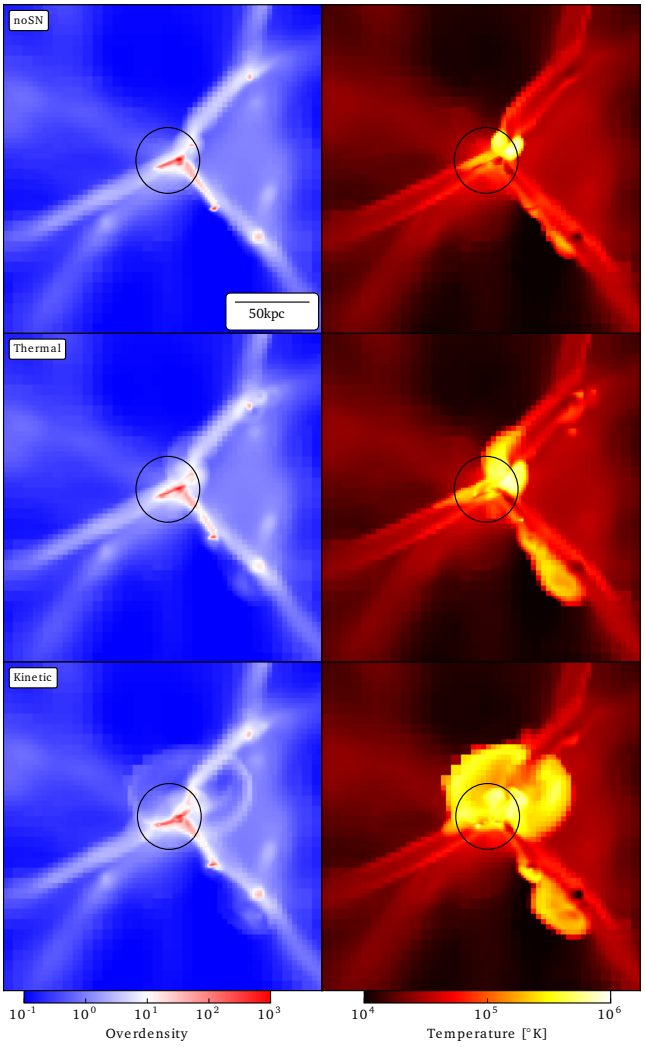

Figure 3. Most massive halo of the simulation (M$\approx 10^{11}$M$_\odot$) at redshift $z = 6$. Average over a 7kpc thick slice of overdensity (left) and temperature (right), without feedback (top), with thermal feedback (middle) and with kinetic feedback (bottom). The black circle represent the $R_{200} = 21$kpc. With the same quantity of energy injected, kinetic feedback can generate much bigger hot bubble ($T > 10^5 K$) around halo than thermal one.

The density map of the *thermal* run is a bit more fluffy around mains over-densities (in red) than the one of the *noSN* run. A thin concentric over-dense region (in white) appears around some halos, for example in the top right filament or around the further over-density in the bottom right filament. These shells are due to the shock of the outflowing gas on the IGM. The main halo is able to generate a bigger hot bubbles (yellow region in temperature maps) in the *thermal* run than in the *noSN* run. Differences also clear on the bottom right filament where a hot bubble was almost absent in the run without feedback.

If we now look at the *kinetic* run, we clearly see a more important impact on both fields than with the thermal injection method. Outflows are significantly stronger and shock shells appear around the main halo with a radius of several R_{200} and a density of about ten times the average density (in white). Furthermore, the hot region is also wider and

corresponds to the inner shock radius defined by the shells in the density map.

The hot region ($T > 10^5$K) in a $5 \cdot R_{200}$ box around the halo represent a volume fraction of $f_V = 0.3\%$ and a total mass of $M_{hot} = 1.9 \cdot 10^9 M_\odot$ for the *noSN* run, compared to $f_V = 1.0\%$ and $M_{hot} = 4.2 \cdot 10^9 M_\odot$ for the thermal run and $f_V = 2.7\%$ and $M_{hot} = 7.3 \cdot 10^9 M_\odot$ for the kinetic run. Around this specific halo, the kinetic feedback can heat 2.7 times more volume and 1.7 time more mass of gas. Despite our limited resolution and our reliance on subgrid models to introduce stellar feedback, it is clear that it has an impact on scales that are in turn resolved in our simulations: its impact on predictions of the large-scale Reionization should therefore be investigated further.

4 STAR FORMATION AND IONIZATION HISTORIES

Cosmological star formation history is first considered: it offers a good global diagnostic of the simulation state, as it considers the whole simulated volume and could be easily compared to observational constraints.

In conjunction, we investigate the cosmic ionization fraction history. We expect a direct link between ionization history and the SFH as ionizing photons are mainly emitted by newly formed stars (see our ionizing emissivity model on Fig. 2a) but we will see that this link is not as direct as expected at the resolution of interests.

In this section we look at how a change in the energy injection model, in the star formation efficiency or in the amount of energy injected influence theses two observables.

4.1 Influence of radiative and supernovae feedback

We want to explore the influence of the energy injection method on the regulation of star formation, so we compare three simulations, one without feedback, one with thermal feedback , and one with kinetic feedback. Theses three simulations are run with radiative processes and with the same initial setup. In addition to these three simulations, we use a reference simulation without radiative sources to measure the influence of radiative transfer feedback.

We observe on Fig 4a that the injection method significantly changes the cosmic SFH. The *Thermal* run (in red) gets a SFR slightly lower than the *noSN* run (in black), and as expected is not as efficient as the kinetic model to regulate star formation. With the same amount of injected energy by unit mass of formed stars, at redshift $z = 6$ the SFR of the *Kinetic* run (in green) is lowered by a factor ≈ 3, compared to the *noSN* run (in black). Star formation processes are dependent of the gas density, which is itself strongly dependent of the resolution. The bump in the SFH at redshift $z \approx 10$ is due to the creation of the last refinement level $L_{max} = 11$ at redshift $Z = 10.6$.

For each methods, the feedback decreases the SFR, so the total number of emitted photons is not the same between simulations. But we observe on Fig. 4b that the Reionization occurs almost at the same redshift in these 3 simulations. The small delay between their reionization redshift is in accordance with their SFH, ie a lower SFH leads to a later reionization. But this delay is smaller than what we could expect just from the lowering of the photon budget. Indeed, at redshift $z = 8$, the kinetic feedback decreases the SFR by a factor ≈ 3 and thus the number of emitted photon is also lowered by approximately the same factor : meanwhile, the ionization rate (given by the slope of the ionization history curve) is surprisingly unaffected. This point is investigated further in section 5.4.

If we only focus on radiative feedback effects, by comparing the differences between the *noFEED* run and the *noSN* run, we can quantify the influence of radiation on the SFH. On Fig. 4a we observe that the *noFEED* run (in black dot) gets almost the same SFH than the *noSN* run (in black). Obviously, the *noFEED* run (black dotted curve on Fig. 4b) do not reionize and stay with an ionization fraction only governed by collisional ionizations. The fact that radiative feedback does not regulate cosmic star formation history implies that it does not influence halos responsible of the global SFH. We will see in section 5 that radiation have an impact on low mass haloes, which are responsible only for a small part of the global SFH.

4.2 Influence of the supernovae feedback efficiency parameter

The supernovae feedback efficiency parameter ϵ_{SN} regroups all the subgrid physics that we do not resolve, such as turbulence or non ionizing radiative energy, reducing the overall energy budget. For that reason ϵ_{SN} has great chances to be lower than the unity and will regulate the quantity of energy effectively injected in the gas at the cell scale.

We run four simulations with different feedback efficiencies ($\epsilon_{SN} = 0$; $\epsilon_{SN} = 10\%$; $\epsilon_{SN} = 50\%$ and $\epsilon_{SN} = 100\%$), and look at how cosmic star formation and ionization histories are impacted by a change in the amount of energy injected. Resulting star formation and ionization histories are presented on Fig. 5. As expected, the more we inject energy, the more we reduce the global SFR (Fig. 5a). Furthermore, we observe the same behavior as the previous section: the regulation of star formation by supernovae feedback does not significantly change the reionization history (Fig. 5b).

We note that the run with the $\epsilon_{SN} = 0.1$ efficiency shows a comparable SFH to the one of the *Thermal* run with 100% efficiency (red curves in both Fig. 4a and Fig. 5a): at our resolution, the thermal feedback scheme presents a 90% of losses compared to the kinetic scheme.

This test does not allows us to conclude about the final quantity of energy to inject, but we observe that if we inject the totality of the energy available from Starburst99 model (the $\epsilon_{SN} = 100\%$ run), the SFR is decreased by a factor ≈ 3 at redshift $z = 6$, which is enough to leave observational constraints.

4.3 Influence of the star formation efficiency parameter

We now explore the link between the star formation efficiency parameter ϵ_{SF} and the supernovae feedback. Indeed, increasing star formation efficiency leads to transforming more gas into stars, and thus increasing the amount of feedback, but increasing the feedback results in decreasing the

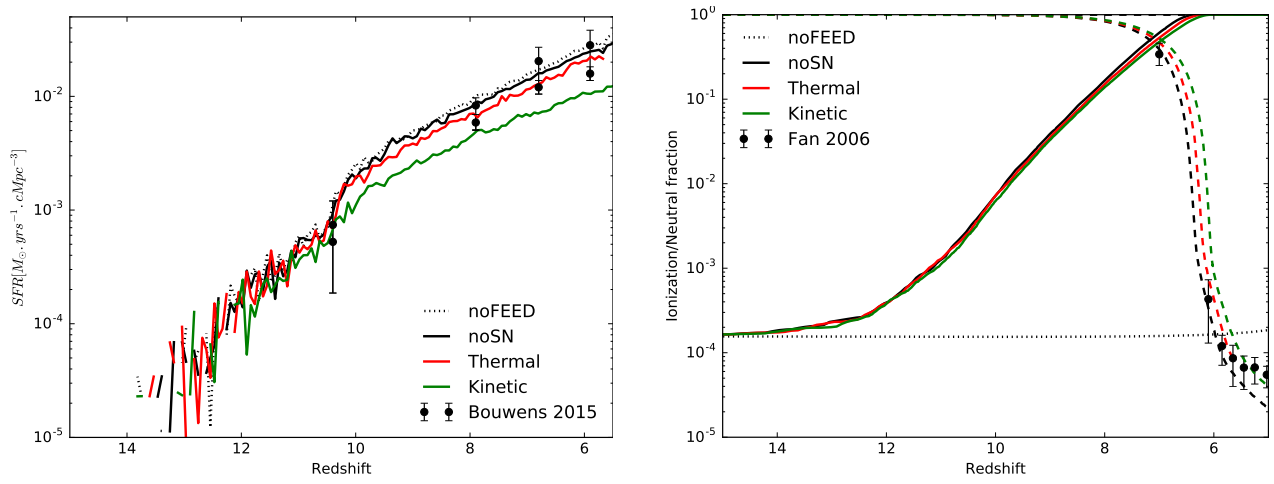

(a) (b)

Figure 4. (a) Cosmic star formation histories and (b) volume weighted ionization (solid lines) and neutral (dashed lines) fraction function of redshift for different feedback method. The introduction of radiation get a small impact on the cosmic SFH. The kinetic method get a significantly stronger effect on the SFH than the thermal model. Reionization occurs almost at the same redshift independently of feedback scheme.

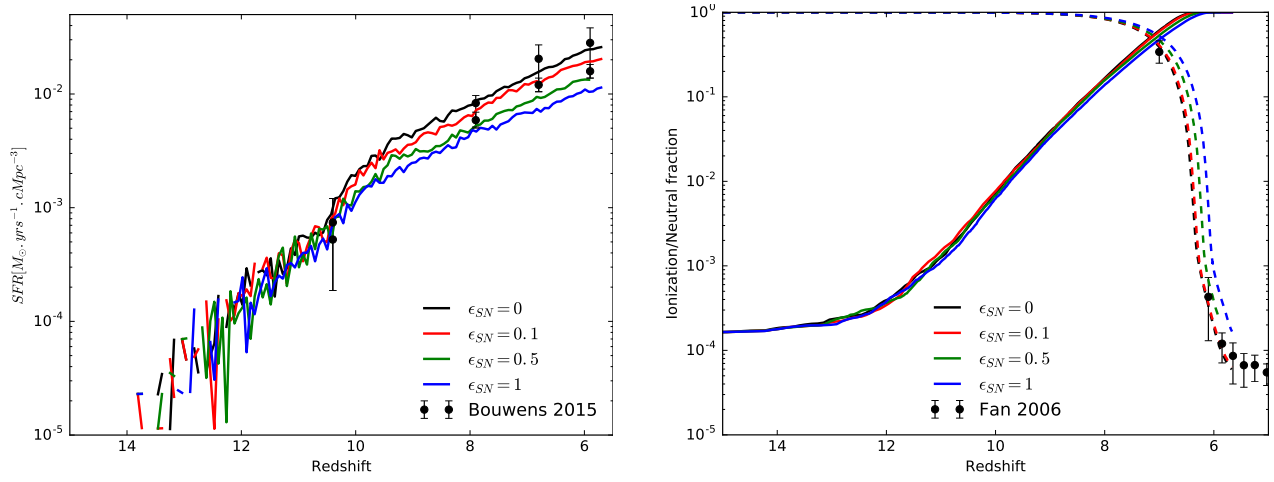

(a) (b)

Figure 5. (a) Cosmic SFH and (b) volume weighted ionization (solid line) and neutral (dashed line) fraction function of feedback efficiency parameter ϵ_{SN} for the kinetic feedback model. The regulation of star formation is directly linked with the quantity of energy injected in the medium. The ionization history is not impacted by the change in the SFH due to supernovae feedback.

star formation rate. It is not clear how the simulation will respond to a change in the star formation efficiency with a given supernovae feedback.

We use the kinetic feedback scheme with an efficiency of ϵ_{SN} = 100% and run three simulations with star formation efficiency of ϵ_{SF} = 0.5%, ϵ_{SF} = 2% and ϵ_{SF} = 10%.

Fig. 6a presents the obtained star formation histories: increasing star formation efficiency leads to first stars at higher redshift and in greater quantity. Later on, the feedback becomes sufficiently strong to change the shape of the SFH.

At high redshift, the SFH seems to be simply regulated by the ϵ_{SF} parameters: the larger ϵ_{SF} is, the more stars are being formed. At later times, the amount of injected energy with high star formation efficiency (ϵ_{SF} = 10%, in blue) becomes sufficient to generate a decreasing star formation history. As increasing feedback do not just shift the whole SFH at lower values but significantly change its shape, we conclude that we cannot fit any arbitrary large SFH, even by increasing the star formation efficiency. It should be noted that the actual efficiency turning-point value is likely to depend on the simulations properties such as the box size and the abundance of massive objects but similar effects were already observed in (Gillet et al., in prep with RAMSES-CUDATON) at similar resolutions.

If we now pay attention to the ionization histories (Fig. 6b), we observe a significant change in the reionization redshift. As expected, the more efficient the star formation is, the sooner the reionization happen. As stars appear sooner in the volume with higher star formation efficiency, the

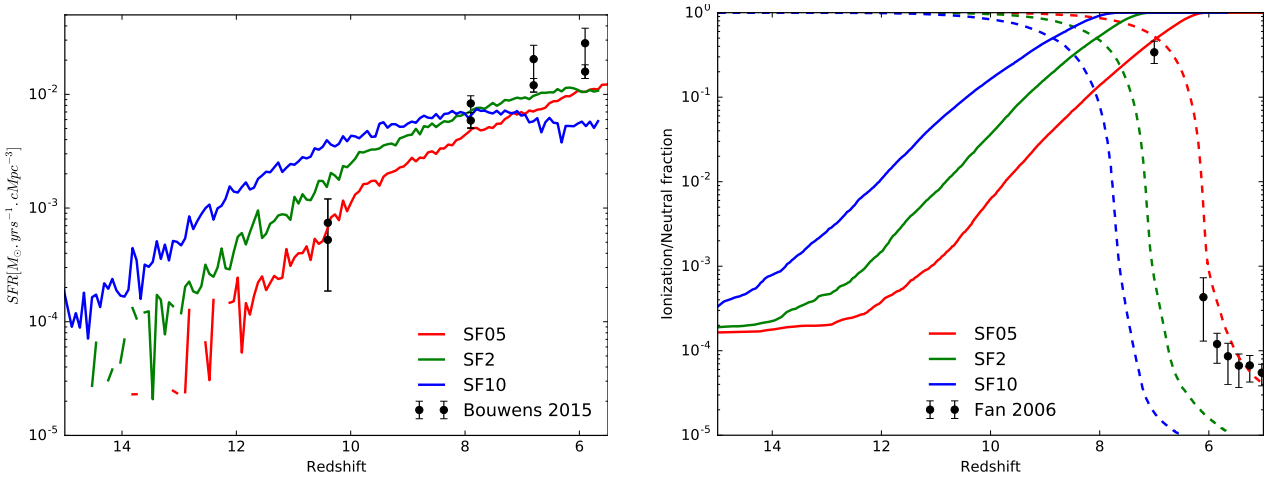

(a) (b)

Figure 6. (a) Star formation and (b) volume weighted ionization histories for different star formation efficiencies ϵ_{SF} with high efficiency ($\epsilon_{SN} = 1$) kinetic feedback. Due to feedback, increasing star formation efficiency can lead to lower the SFR.

medium starts to reionize at higher redshift. But as the feedback needs time to be efficient at regulating the SFR, it also needs time to regulate the ionization rate.

There is a small change in the slope of the *SF10* ionization curve (in blue on Fig. 6b) after redshift $z \approx 11$, due to the decrease of the SFR. But the effect of feedback do not seems to be sufficient to stop the reionizing processes, at least in the range of parameters we explore. However, it may be possible that the SFR cutout will be sufficient to keep the box away from reionizing if we push the efficiency further.

5 HALO-CENTRIC STUDIES

5.1 Halos and galaxies mass function

We now focus on the properties of the halo population. Halos are detected using the Friends-Of-Friends algorithm of PFOF (Roy et al. 2014) providing ~ 18000 objects with a least 10 particles.

Stars are associated to a halo if they are within its R_{200}. The R_{200} defined as the radius where the average density of the halo correspond to 200 times the average dark matter density:

$$R_{200} = \left(\frac{3 \cdot M_{fof}}{4\pi \cdot 200\bar{\rho}} \right)^{1/3}, \quad (7)$$

with $\bar{\rho} = (\Omega_m - \Omega_b)\frac{3H_0^2}{8\pi G}$ the average dark matter density in the universe and M_{fof} the halo mass given by PFOF.

The z=6 halos and galaxies stellar mass functions (HMF/GSMF) are presented on Fig. 7. GSMF are compared to data from Song et al. (2016). We observe no measurable impact on the HMF function of the feedback type. While radiation seems to be almost neutral on the number of galaxies, the GSMF is significantly reduced by supernovae feedback.

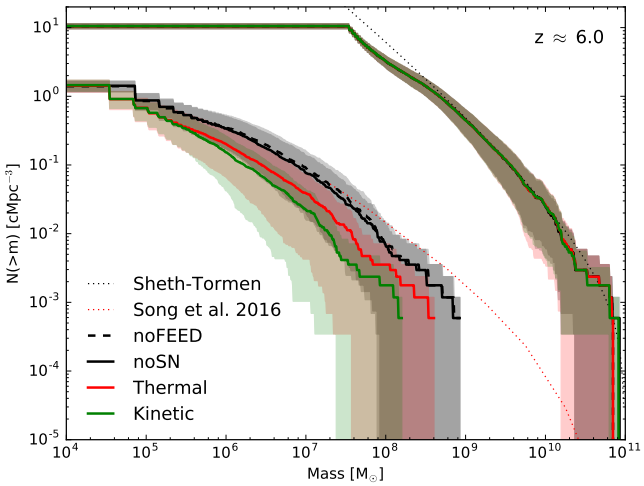

Figure 7. Cumulative halos and galaxies stellar mass function (HMF/GSMF) for different feedback types and 100% efficiency at redshift z=6. The feedback does not change the HMF, but has an influence on the GSMF.

5.2 Star formation and baryon fraction

The balance between star formation and feedback, functions of halo mass, is not trivial. Indeed, low masses halos ($M < 10^9 M_\odot$) do not form much stars (mostly because they are easily photo-suppressed) and thus are not exposed to a large amount of feedback. However if a stellar population forms in these light halos, supernovae events can expel a significant part of the gas. On the other side, high masses halos ($M > 10^{10} M_\odot$) host large star formation events and are exposed to strong feedback processes, but their gravitational potential is much more able to keep their baryon in.

Moreover low-mass halos ($M < 10^9 M_\odot$) are predominant in number but they get a lower SFR, so they do not host large quantity of UV emitting stars.Conversely, high-mass halos do emit a strong UV field but are far less numerous. What are the respective contributions of each classes

of masses on the photons budget and how this budget is influenced by feedback?

We compute instantaneous star formation rate for each halo by measuring the total stellar mass appeared within its R_{200} during the last 10Myr :

$$SFR_{10}^{halo} = \frac{\sum M_\star \left(r < R_{200}^{halo}; t < 10\mathrm{Myr}\right)}{10\mathrm{Myr}}. \quad (8)$$

The correlation between the halo mass and its instantaneous SFR is presented on Fig. 8a. In all cases, the introduction of feedback leads to decreasing the SFR and change the slope of this correlation. Radiative (in plain black) and thermal feedback (in red) tend to be more efficient at lowering the SFR for low masses halos ($M < 10^9 M_\odot$) while kinetic feedback (in green) tends to act on heavy halos ($M > 10^{10} M_\odot$).

If we now look at SFR_{bin}, the total contribution of a class of halos masses to the cosmic SFR:

$$SFR_{bin} = \sum_{halo} SFR_{10}^{halo} \left(M_{bin} \leq M^{halo} < M_{bin} + dM\right), \quad (9)$$

presented on Fig. 8b, we see that smallest halos ($M < 10^9 M_\odot$), do not represent a significant fraction of the global SFR at this time, even if they are the most numerous. Meanwhile, halos around $10^{10} M_\odot$ are the main contributors of the cosmic SFR at $z = 6$. For the *noFEED* run, the cumulative SFR seems to decrease for halos heavier than $10^{10} M_\odot$, however, it is not clear if it is a statistical effect due to the limited size of the simulation or a physical effect. Independently of the feedback type, halos under $10^9 M_\odot$ are not the main contributors of the SFR and thus of the UV photon budget at $z = 6$. To alter the cosmic SFH, a feedback scheme has to change SFR in the predominant class of halos masses. We see from Fig 8a that kinetic injection is the most efficient to regulate star formation in this range of masses ($M > 10^{10} M_\odot$), and thus the most efficient to regulate the global SFR.

The main quantity responsible to the SFR is the gas density (see Eq. 1), so an efficient feedback should break over-densities responsible for stars formation. And as these over-densities are located in halos, we expect that the decrease in the halo's SFR is due a diminution of the quantity of baryon belonging to it. We observe that the averaged baryon fraction for a class of masses (Fig. 8c) is linked to the SFR. For all ranges of masses, the lower the baryon fraction is, the less the SFR is. This is particularly clear for halos with masses over 10^{10}M$_\odot$: the SFR is not impacted by thermal feedback (in red) and the baryon fraction is almost universal, but for kinetic feedback (in green) we observe a diminution of the baryon fraction and therefore of the SFR.

5.3 Average R_{200} flow speed

In this section, we investigate the evolution of the average radial velocity of the gas around halos depending on the feedback scheme. To compute these velocities, we draw a virtual sphere around each halo with a given radius and centered on the center of mass of the halo. The resulting velocities are a function of the distance from the halo. Here we arbitrary take R_{200} as our reference radius.

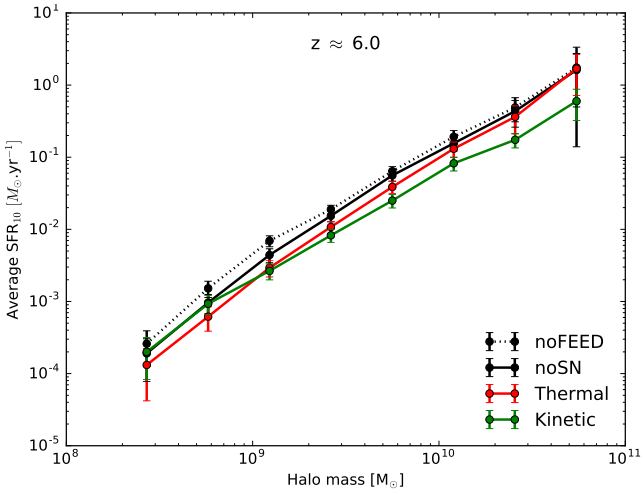

(a)

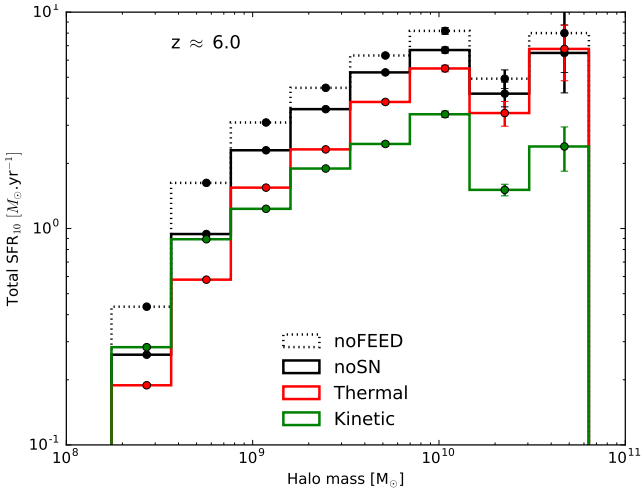

(b)

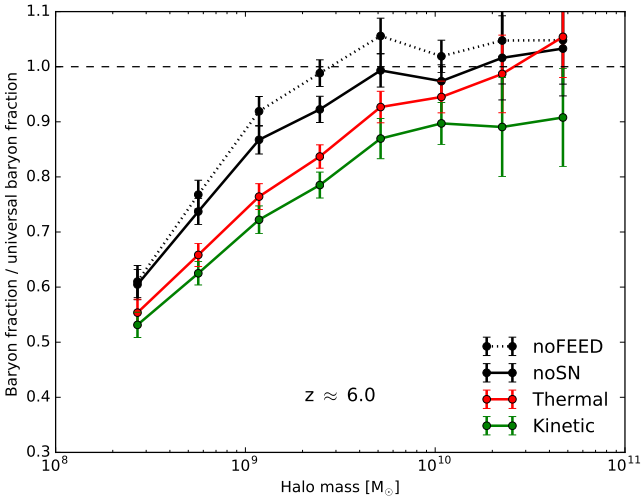

(c)

Figure 8. Star formation rate averaged (a), binned (b) and average baryon fraction (c) by bins of halo mass at redshift z=6 for different feedback methods. Thermal feedback tend to have impact on smallest halos, while kinetic form reduce the SFR on the biggest one. Halo with masses around $10^{10} M_\odot$ are responsible of the major fraction of the global SFR, and thus of the photon budget.

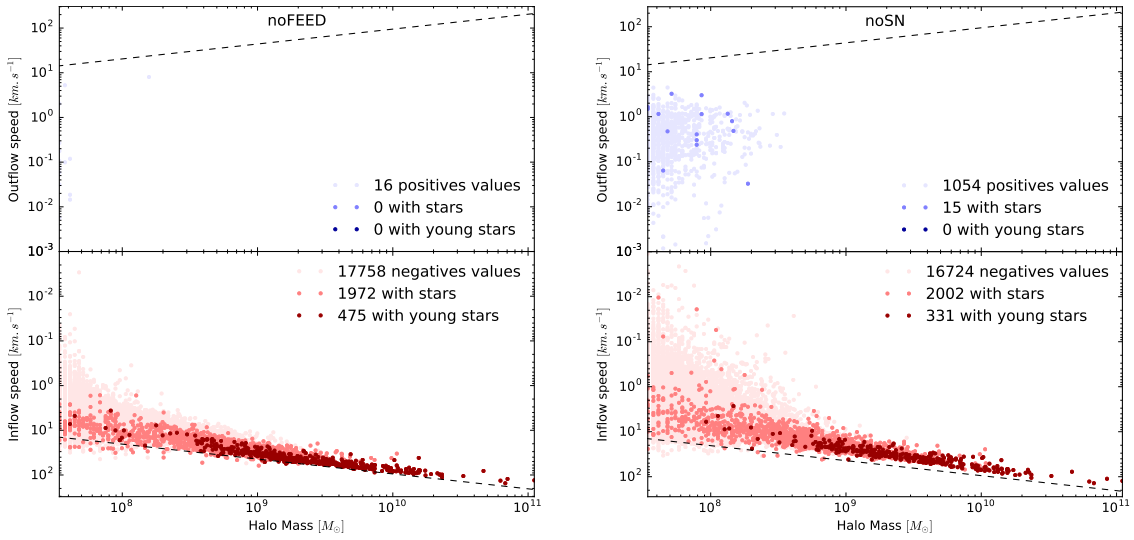

(a) Without feedback

(b) Radiative transfert (RT) only

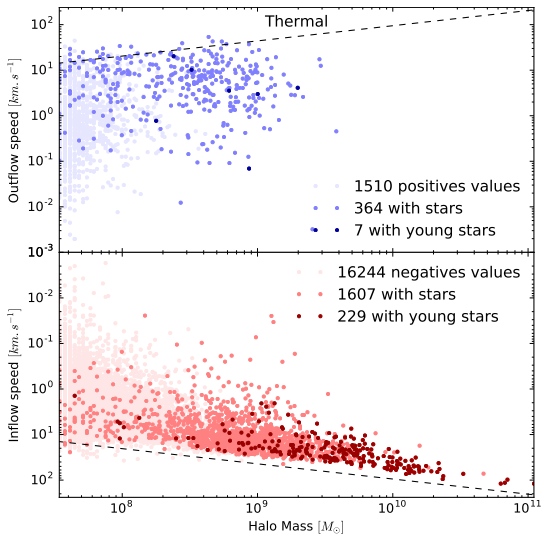

(c) RT + thermal SN

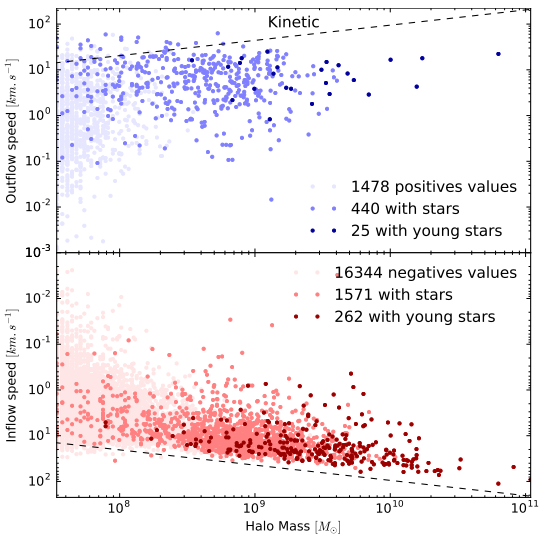

(d) RT + kinetic SN

Figure 9. Average radial hydrodynamical flow speed at R_{200} function of injection method measured at redshift z=6. Blue dots represent halos with outflow, red with inflow. Light dots represent halos without stars while dark dots stand for halos with stars. The dashed line represents ± the escape velocity. Without radiation there is almost no halo with a positive average speed (outflowing matter). The introduction of radiation leads to the apparition of a population of starless low mass halos ($M < 3 \cdot 10^8 M_\odot$) with outflow. Supernovae introduce a population of outflowing halos with stars. Kinetic feedback allows heavier halos to get outflow than thermal feedback.

The general expression for the average radial velocity $\bar{v}$, is:

$$\bar{v} = \frac{\oint \vec{v} \cdot d\vec{s}}{\oint d\vec{s}}, \tag{10}$$

with $d\vec{s}$ the surface element of the R_{200} sphere. Each sphere is discretized with 3072 HEALPix points (Górski et al. 2005), the average radial velocity became:

$$\bar{v} = \frac{1}{N} \sum_{i=1}^{N} \vec{v_i} \cdot \vec{r_i}, \tag{11}$$

with N the number of HEALPix points, $\vec{v_i}$ the gas velocity of the nearest cell of point i and the normal vector $\vec{r_i}$ oriented outward. Therefore, positive values stand for outflow and negatives one for inflow. Fig. 9 presents the resulting average velocities as a function of halo masses for the different feedback schemes. Each halo is represented by a dot, with a different color depending if it has stars, young stars ($t_* < t_{life}$) or no star. The upper part of the diagram represents outflows and the lower part represents inflows.

The dashed lines are defined by:

$$v_{lim} = \pm\sqrt{\frac{2GM_{(r<R_{200})}}{R_{200}}}, \tag{12}$$

and represent the free fall velocity limit for the inflowing case, and the escape velocity for the out-flowing case.

Without feedback (Fig. 9a) almost all halos are in the negative part of the diagram, they are all accumulating baryons. The correlation between inflow speeds and halo masses is particularly sharp with this run, and at this redshift ($z = 6$).

This free fall tendency tends to be an upper limit of the accretion velocity, and only few halos have average inflow velocity with an absolute value over this limit. Also, we note that the velocity dispersion became wider as halos became less massive.

With the introduction of radiation (Fig. 9b), there is an increase in the dispersion of velocity values. This increase is more pronounced on halos lighter than $3 \cdot 10^8 M_\odot$ and specially starless ones (light red population) at a point that a part of this population starts to get net outflows (in light blue). The fact that the major part of this population do not have stars, says that theses outflows are not due to internal feedback, and suggest an external effect. Our interpretation is that these light halos are submitted to a UV field created by surrounding halos massive enough to get a significant amount of young stars. We are observing the effect of photo-heating by radiative feedback, the gas heated by radiation expands and leaves its host by dilution. Meanwhile, heavier halos can hold their baryons thanks to their deeper potential.

With an average speed of $\approx 0.5\text{km.s}^{-1}$ theses outflows are relatively slow and all velocities are below the escape velocity, so baryon are still bounded to their host.

We show in Sec. 4.1 that radiation have a negligible impact on the cosmic SFR, but we observe here that it can generate outflows for low masses halos. These two points are not in contradiction, as we show in Sec. 5.2 that these low masses halos represent a small part of the global SFR in our simulations. So radiation do have an impact on star formation but only on halos with a small contribution to the global star formation.

There is also a small shift, present for almost all the halos masses range, in inflowing speeds: inflows tend to be slightly slower due to photo-heating. Radiation generates outflows and slow down the collapse of gas, reducing the quantity of available star forming material by limiting the accretion.

If we now focus on the two runs with supernovae feedback (Fig. 9c and 9d), we clearly see that there is a new population of halos with outflows and that almost all those halos have stars (dark blue). Supernovae feedback also limit the accretion, the dispersion of inflowing halos with stars (dark red) is significantly increased. This idea is supported by the fact that the distribution of starless halos stay mainly unchanged compared to RT only run (Fig. 9b).

The mean outflow speed is now close to 10km.s^{-1} which is twenty times greater than for the *noSN* run. Some light halos ($M < 10^9 M_\odot$) present an average outflow speed greater than the escape velocity: the feedback is able to disperse material out of these objects. It seems that the feedback type does not change the maximum outflow speed ($\approx 60\text{km.s}^{-1}$), while only large halos present a positive average speed. The most massive halo with outflow in the *noSN* simulation weight $3.5 \cdot 10^8 M_\odot$, $3.6 \cdot 10^9 M_\odot$ in the *thermal* run and $6.3 \cdot 10^{10} M_\odot$ in the *kinetic* run. Outflow velocities can seem low compared to observed ones (between ≈ 20 and $\approx 2000\text{Km.s}^{-1}$ according to Veilleux et al. (2005)) but we are considering averaged values: locally on the virial spheres, velocities can be as high as 600km.s^{-1} at the R_{200} level, and 1500km.s^{-1} in a cell where the explosion occurs, which is in the typical range of observed velocities.

5.4 Influence of supernovae feedback scheme on R_{200} halo emissivity

In this section we want to quantify how does the emissivity of halos change as a function of the supernovae energy injection scheme.

Due to the moment based treatment of radiation, we can use a procedure similar to our hydrodynamical analysis (Sec 5.3) to compute F_{200}, the halo emissivity at R_{200}, by integrating the radiative flux field $\vec{F}_{rad}$ for each halo:

$$F_{200}^{halo} = \oint_{R_{200}^{halo}} \vec{F}_{rad} \cdot d\vec{s}. \tag{13}$$

Also, in a similar way that in Eq. 9, we can sum these F_{200} by masses bins, and estimate the photon budget distribution:

$$F_{bin} = \sum_{halo} F_{200}^{halo} \left(M_{bin} \leq M^{halo} < M_{bin} + dM \right). \tag{14}$$

Fig. 10a presents F_{bin}, the total emissivity of halos in a range of masses for our three feedback schemes.

First, it appears that there are two regimes in this diagram: most massive halos represent the biggest part of the emissivity while lightest ones contribute about ten times less. Also, it seems that the total emissivity of heavier halos tends to decrease with the halo mass, however it is not clear if it is a physical effect or a statistical effect due to the box size we are considering $(\approx 12\text{ cMpc})^3$ and the low abundance of such massive haloes.

We have to take into consideration that we are using the Coarse Radiative Transport Approximation (CRTA), ie the radiative transport computations are only executed on the coarsest grid. At the scale of a coarsest cell, the radiation field can be considered as a homogeneous UV background. The dashed line represents $M_{min} = 3.3 \cdot 10^9 M_\odot$, the mass of a halo with R_{200} equals to the radiative transport resolution limit.

Halos with masses over M_{min} are responsible of the major part of the photon budget of our simulations. Approximately 80 % of photons are coming from theses halos :

$$\frac{\sum \dot{N}(M > M_{min})}{\sum \dot{N}} \approx 80\%, \tag{15}$$

with $\dot{N}$ the stellar particle emissivity belonging to the current halo, and for those ones, the feedback scheme does almost not change the total emissivity at the R_{200} level (Fig. 10a). We observe in Sec. 4.1 and more particularly on Fig. 4, that the feedback scheme do not change reionization history, we now understand that this is because feedback does not change the halo F_{200} emissivity.

Moreover the order of theses curves is in accordance with the order found in Fig. 4b: the F_{200} halo emissivity of the kinetic run is slightly lower than the two other runs, and so its reionization happens last.

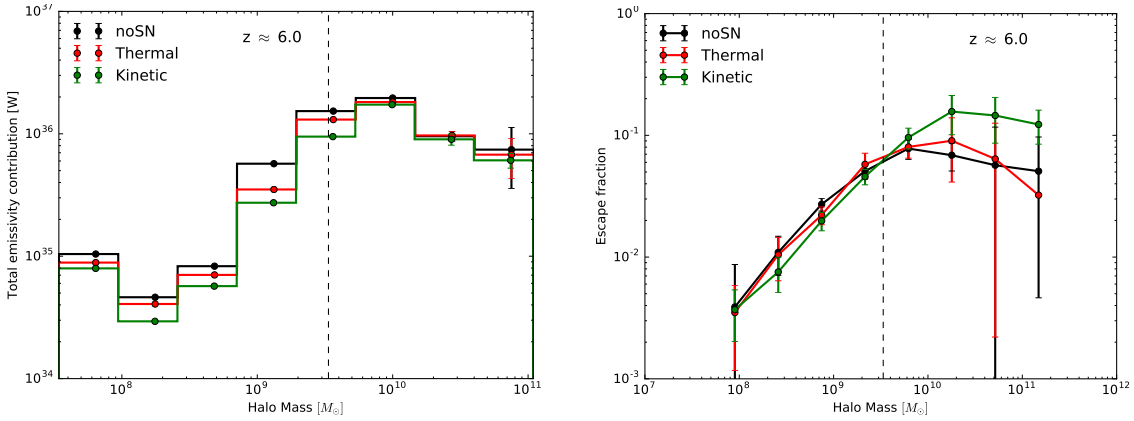

(a) Total R200 emissivity

(b) Estimated average escape fraction

Figure 10. Total R_{200} emissivity contribution (a) and escape fraction (b) as a function of halo mass, for different feedback scheme. All measures are done at redshift z=6. The dashed line represents the halo mass equivalent to our radiative resolution limit. For massive ($M > 10^{10} M_\odot$), radiatively well resolved halos, emissivity stays almost identical independently of the feedback scheme. We observe a significant increase in the escape fraction of massive halos with the kinetic scheme.

If we finally compute the ratio of these F_{200} halos emissivities to $\dot{N}$ their internal radiative sources (directly linked to the integrated SFR presented in Fig. 8b), we obtain a rough estimation of f_{esc}, the photon escape fraction. The escape fraction is computed using prescription of (Kimm et al. 2017), ie we consider the time needed by photons to travel from the halo center to R_{200}:

$$f_{esc} = \frac{F_{200}}{\sum \dot{N}_{\left(t - \frac{R_{200}}{c}\right)}}. \tag{16}$$

Fig. 10b presents this averaged escape fraction as a function of halo masses.

For halos under M_{min}, the observed linearity of the relation is due to a purely numerical effect. For these halos, the flux value became independent of the radius of the computation (as it stays constant within a given cell), and as the halo surface goes with the square of the R_{200} : $\left(S \propto R_{200}^2\right)$ and the halo mass with the third of the R_{200} : $\left(M \propto R_{200}^{1/3}\right)$ it results in a power two third relation between the F_{200} flux and the halo mass: $\left(F_{200} \propto R_{200}^{2/3}\right)$.

If we now focus on the well resolved part of the diagram, we observe an increase of the escape fraction for heaviest halos ($M > 10^{10} M_\odot$) for the kinetic feedback scheme. This explains how the run with kinetic feedback reionize as quickly as other runs, despite its lower SFR: massive halos form less stars but they are more efficient at releasing their photons into the IGM.

The increase of photon escape fraction by supernovae feedback we measure confirm previous works such as eg Kimm & Cen (2014) or Trebitsch et al. (2015). This rise in the escape fraction means that the escaping way of photon is easier, and so that the probability of photon interaction with baryon is lower. If we compare the evolution of the escape fraction to the measured baryon fraction (Fig. 8c), we observe that when baryon fraction is reduced, the escape fraction tends to be higher and vice versa.

6 CONCLUSION

In the previous sections we discussed the impact of supernova and radiative feedbacks on simulations of the Reionization process. The level of approximation and resolution envisioned here is the one used in large scale simulations of the process : in-situ physics of the impact of feedback within galaxies cannot be fully captured but the focus is put on the diversity of situations with halo populations where e.g. environmental effects are included such as the photo-suppression of star formation by external radiation.

For this purpose, we present a simple scheme of supernovae energy injection in AMR cosmological simulation of reionization. We test this model by running a set of fully coupled radiative hydrodynamic simulations, varying feedback implementation and model free parameters. We show that this feedback scheme is able to regulate star formation and generate galactic winds on a wide range of halo masses.

Our main results can be summarized as follows.

- Runs with radiation produce a population of low mass ($M < 10^9 M_\odot$) halos with outflowing gas (Fig. 9b). We interpret this population as photo-heated halos, losing their baryons by photo-evaporation.
- Even with a strong regulation of star formation and thus of the photon budget, the supernovae feedback scheme does not change the reionization history in our simulations, despite a strong impact on the SFR. Indeed, we measure the quantity of radiative energy escaping through halos virial radii and show that it does not depend on supernovae feedback (Fig. 10a). We interpret this behaviour by the expulsion of baryons by feedback, create easy escape path for the radiation. So, even with a strong regulation of the SFR, and thus of the number of emitted photons, this increase of the escape fraction leads to a comparable number of photons reaching the IGM and thus a similar reionization history.
- The escape fraction of photons of halos with masses over $10^{10} M_\odot$ is increased by a factor ≈ 3 by our kinetic feedback scheme.
- As a consequence, we find that the photon budget is mainly governed by massive halos ($M > 10^9 M_\odot$) (Fig. 10a).

Simulation like CODA will be used to improve statistics in the range $10^{10}M_{\odot} < M < 10^{11}M_{\odot}$ and explore if the decrease in photon budget for halos more massive than $10^{10}M_{\odot}$ observed in Fig 10a is still present or not. A GSMF better sampled can leads to two scenario:

- either our small boxes are converged and this decrease still exist. In this eventuality, the photon budget of this kind of simulations is mostly governed by halo of masses $M \approx 10^{10}M_{\odot}$. Our main constraint on the reionization is governed by the average ionization state at cosmic scales. Small boxes do not sample the variety of density fluctuations needed to obtain the convergence on the average ionization state. But if we correctly sample the most predominant radiative sources, presented results can stay valuable outside a pure comparative purpose. In this case we should mostly focus on the first phase of the reionization, where light escape from sources and do not reach the cosmic voids yet, when considering small boxes studies.
- either our small boxes are not converged and the photon budget will continue to rise with the halo mass. This case means that we do not have a sufficient galaxies statistic, and that sources are not correctly sampled. If the drop is still present at the high mass end of big runs, it will be necessary to run even bigger simulations until obtaining the convergence. It also means that big productions runs could never be calibrated using smaller simulation, the photon budget will be governed by halos of masses that is not sampled in calibrations runs.

Preliminary CODA analyses tend to be in favour of the first scenario, and it seams that $64cMpc^3$ boxes also present a maximum in the photon budget around a halo mass of $10^{10}M_{\odot}$.

ACKNOWLEDGEMENTS

This work is supported by the ANR ORAGE grant ANR-14-CE33-0016 of the French Agence Nationale de la Recherche.

REFERENCES

Aubert D., Teyssier R., 2008, Monthly Notices of the Royal Astronomical Society, 387, 295
Aubert D., Teyssier R., 2010, ApJ, 724, 244
Aubert D., Deparis N., Ocvirk P., 2015, Monthly Notices of the Royal Astronomical Society, 454, 1012
Bouwens R. J., Illingworth G. D., Oesch P. A., Caruana J., Holwerda B., Smit R., Wilkins S., 2015, The Astrophysical Journal, 811, 140
Chardin J., Puchwein E., Haehnelt M. G., 2017, Monthly Notices of the Royal Astronomical Society, 465, 3429
D'Aloisio A., Upton Sanderbeck P. R., McQuinn M., Trac H., Shapiro P. R., 2016, preprint, 1607, arXiv:1607.06467
Dalla Vecchia C., Schaye J., 2012, Monthly Notices of the Royal Astronomical Society, 426, 140
Dubois Y., Teyssier R., 2008, Astronomy and Astrophysics, 477, 79
Giallongo E., et al., 2015, Astronomy and Astrophysics, 578, A83
Gnedin N. Y., 2014, arXiv:1403.4245 [astro-ph]
Górski K. M., Hivon E., Banday A. J., Wandelt B. D., Hansen F. K., Reinecke M., Bartelmann M., 2005, ApJ, 622, 759
Haardt F., Madau P., 2012, The Astrophysical Journal, 746, 125
Hahn O., Abel T., 2011, Monthly Notices of the Royal Astronomical Society, 415, 2101
Hockney R. W., Eastwood J. W., 1981, Computer Simulation Using Particles
Iliev I. T., Mellema G., Ahn K., Shapiro P. R., Mao Y., Pen U.-L., 2014, Monthly Notices of the Royal Astronomical Society, 439, 725
Katz N., 1992, The Astrophysical Journal, 391, 502
Kennicutt J., 1998, The Astrophysical Journal, 498, 541
Khokhlov A., 1998, Journal of Computational Physics, 143, 519
Kimm T., Cen R., 2014, The Astrophysical Journal, 788, 121
Kimm T., Cen R., Devriendt J., Dubois Y., Slyz A., 2015, arXiv:1501.05655 [astro-ph]
Kimm T., Katz H., Haehnelt M., Rosdahl J., Devriendt J., Slyz A., 2017, Monthly Notices of the Royal Astronomical Society
Leitherer C., et al., 1999, The Astrophysical Journal Supplement Series, 123, 3
Li T. Y., Alvarez M. A., Wechsler R. H., Abel T., 2014, ApJ, 785, 134
Navarro J. F., White S. D. M., 1993, Monthly Notices of the Royal Astronomical Society, 265, 271
Ocvirk P., et al., 2015, preprint, 1511, 11
Planck Collaboration et al., 2015, preprint, 1502, arXiv:1502.01589
Rasera Y., Teyssier R., 2006, Astronomy and Astrophysics, 445, 1
Rosdahl J., Schaye J., Dubois Y., Kimm T., Teyssier R., 2016, preprint, 1609, arXiv:1609.01296
Roy F., Bouillot V. R., Rasera Y., 2014, Astronomy and Astrophysics, 564, A13
Song M., et al., 2016, ApJ, 825, 5
Springel V., Hernquist L., 2003, Monthly Notices of the Royal Astronomical Society, 339, 289
Stinson G., Seth A., Katz N., Wadsley J., Governato F., Quinn T., 2006, Monthly Notices of the Royal Astronomical Society, 373, 1074
Toro E. F., 1997, Riemann solvers and numerical methods for fluid dynamics : a practical introduction. Springer, Berlin, New York, http://opac.inria.fr/record=b1093563
Trebitsch M., Blaizot J., Rosdahl J., 2015. eprint: arXiv:1510.06949, pp 105–108, http://adsabs.harvard.edu/abs/2015sf2a.conf..105T
Veilleux S., Cecil G., Bland-Hawthorn J., 2005, Annual Review of Astronomy and Astrophysics, 43, 769
Wise J. H., Cen R., 2009, ApJ, 693, 984

This paper has been typeset from a TEX/LATEX file prepared by the author.